ADVANCED FUNCTIONAL MATERIALS
www.afm-journal.de

Emerging In Situ and Operando Nanoscale X-Ray Imaging Techniques for Energy Storage Materials

Johanna Nelson Weker and Michael F. Toney**

Electrical vehicles (EVs) are an attractive option for moving towards a CO_2 neutral transportation sector, but in order for widespread commercial use of EVs, the cost of electrical energy storage (i.e., batteries) must be reduced and the energy storage capacity must be increased. New, higher performing but Earth abundant electrodes are needed to accomplish this goal. To aid the development of these materials, in situ characterization to understand battery operation and failure is essential. Since electrodes are inherently heterogeneous, with a range of relevant length scales, imaging is a necessary component of the suite of characterization methods. In this Feature Article, the rapidly growing and developing field of X-ray based microscopy (XM) techniques is described and reviewed focusing on in situ and operando adaptations. Further, in situ transmission electron microscopy (TEM) is briefly discussed in this context and its complement to XM is emphasized. Finally, a perspective is given on some emerging X-ray based imaging approaches for energy storage materials.

1. Introduction

Global climate change is widely accepted within the scientific community. Consequently, limiting the atmospheric carbon dioxide induced temperature rise is currently one of the greatest challenges facing humanity. There are a number of approaches for developing a sustainable carbon-neutral energy infrastructure.[1] These all require large scale use of energy storage for transportation and "grid level" renewable energy generation – portable and stationary, respectively. Electrical vehicles (EV) require on-board storage of large extents of energy for long cruising range. Sustainable energy generation sources (e.g., wind and solar) are intermittent requiring large storage capabilities to balance supply and demand. Due to its high capacity, electrochemical energy storage (e.g., batteries) offers the best technology, especially for portable storage, and is a viable contender for grid storage. However, the present technologies lack adequate energy storage capacity, are expensive, and potentially unsafe. While batteries have improved over time, the historic rate of increase in capacity is a meager ≈3% per year,[2] which constituents a "Moore's law" for energy storage. Li-ion battery (LIB) technologies currently offer the best performance for EV applications (and for portable electronics) due to their high energy density. LIBs were developed through the 1970s by solid state electrochemists and were commercially implemented by Sony in 1991.[3] Over nearly 25 years the storage capacity has increased by more than a factor of two (from 90 Wh/kg to 210 Wh/kg). However, for the widespread implementation of energy storage, we must dramatically improve the existing technologies – both in terms of capacity and cost. The estimated capacity and cost required are 500–600 Wh/kg[2] at a cost of $125 /kWh[4] for EVs.

LIBs operate in a "rocking chair" mode by shuttling electrons and Li ions back and forth between an anode (negative electrode) and cathode (positive electrode), with the electrons flowing through current collectors and an external load and the ions migrating through the electrolyte and a separator. While all aspects of the battery need to be improved, the anode and cathode are receiving tremendous attention as these largely determine the storage capacity and cost. As shown in **Figure 1**, electrodes can be classified by their Li storage mechanism in terms of insertion, alloying, or conversion.[5] Most electrodes in present day LIBs make use of insertion reactions, where Li inserts or intercalates into an electrode host lattice. This includes the widely used graphite anodes (Li intercalation in between graphite sheets) and $LiCoO_2$ cathodes (Li insertion into octahedral sites in the $LiCoO_2$ lattice). These reactions can be either heterogeneous (e.g., two phase) or homogeneous, but are typically low capacity as there is only half an electron transferred per metal atom (e.g., Co in $LiCoO_2$). In the alloying reaction mechanism, Li forms an alloy with a metal or semiconductor such as Si, Ge or Sn anodes. Alloying electrodes often have huge capacities (e.g., Si → $Li_{4.4}Si$, accommodating more than four Li per Si), but there is a concomitant huge volume expansion (ca. 300–400%), which results in loss of electrode integrity and rapid capacity fading. A conversion reaction involves Li reacting with a parent compound (often a transition metal oxide or sulfide) which decomposes, resulting in metal embedded in a Li compound (e.g., Li_2O). This case includes oxides, such as Fe_3O_4, and even sulfur cathodes (sulfur converts

Dr. J. Nelson Weker, Dr. M. F. Toney
Stanford Synchrotron Radiation Lightsource
SLAC National Accelerator Laboratory
Menlo Park, CA 94025, USA
E-mail: jlnelson@slac.stanford.edu;
mftoney@slac.stanford.edu

DOI: 10.1002/adfm.201403409

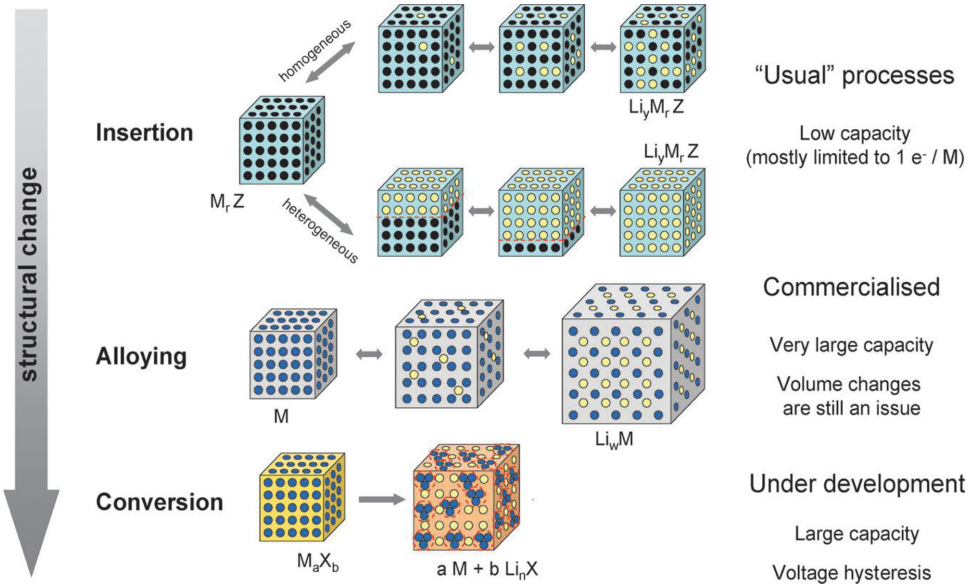

Figure 1. Different electrode lithiation storage mechanisms: insertion, alloying, and conversion. Reproduced with permission.[5] Copyright 2009, The Royal Society of Chemistry.

to Li_2S). Conversion electrodes involve multiple electrons and hence can have high capacities. Li-air[6] can be considered one implementation in which the cathode is just atmospheric oxygen, resulting in a potential storage capacity approaching that of gasoline, at least in theory.

Present LIBs typically use graphite as the anode and a transition metal oxide, such as $LiCoO_2$ (resulting in a capacity of 130 mAh/g) or $LiNi_{1/3}Co_{1/3}Mn_{1/3}O_2$ (150 mAh/g), as the cathode. The need for dramatic improvements in capacity drives the research and development of new, much higher capacity (but inexpensive) electrode materials both experimentally[7] and theoretically.[8] However, to fully understand and develop new materials, we must understand how these materials operate in batteries during charging and discharging, especially the reaction pathways and morphological (particle shape) changes. This necessitates approaches using in situ and operando characterization to watch electrode operation and failure. This is part of the "materials by design" paradigm in which theory guides synthesis, validated by characterization, in a feedback fashion.

Practical batteries and their constituent electrodes are inherently complex, heterogeneous systems consisting of electrochemically active materials, binders, electrolyte, and (wanted and unwanted) reaction products. Further, the transient and non-equilibrium nature of electrode materials and processes makes them challenging to characterize. These factors have all contributed to the slow progress historically made in improving LIBs (e.g., the 3%/year "Moore's law"). One challenge is that understanding electrodes often requires spatially resolved in situ imaging of these components at a range of length and time scales, which requires a multi-modal approach. This is illustrated in **Figure 2**, which shows in situ and operando imaging techniques, the probed length scale (on horizontal axis), and the type of in situ cell used (vertical axis). It is clear that access to the range of electrode-relevant length scales (Å to mm) requires a number of techniques or modes.

To remove any ambiguity in the often imprecise use of the terms in situ and operando, these terms will be defined here in the context of electrochemical energy storage. Operando characterization is reserved for experiments when the material is within a battery under typical biasing and operating conditions, although not necessarily a fully functioning device (e.g., a half cell). In situ refers to measurements in the relevant environment (e.g., in an electrolyte and under bias) but not necessarily operating. "Relevant" is a subjective term and can include a battery under atypical or very unusual biasing. An example of this characterization would be the rapid constant voltage biasing of single particle batteries performed in transmission electron microscopes (TEM). These results are valuable in understanding lithiation processes, but may not be directly transferable to the standard constant current biasing of batteries containing many particles. A material under investigation within a battery cell, but not under active biasing can also be termed in situ, but with the qualifier "not under bias".

It is useful to briefly describe the in situ and *operando structure* and morphology characterization techniques that are often used for energy storage materials and to note what information these provide, and their strengths and weaknesses. A list appears on **Table 1**, along with the (predominant) property probed. Spatially averaging techniques that are sensitive to local and long range atomic order and structure include X-ray diffraction (XRD),[9] X-ray absorption spectroscopy (XAS),[10] neutron diffraction,[11,12] nuclear magnetic resonance (NMR),[13] and Fourier transform infrared spectroscopy (FTIR).[14] For imaging, Figure 2 shows spatially resolved in situ imaging techniques and indicates the spatial resolution of each approach along with the type of cell used. Atomic force microscopy (AFM)[15] provides surface topography and been used to measure the large volume changes of lithium alloying films during cycling. Neutron imaging has been used to observe a full battery operando, but with a >10 μm scale resolution.[12,16]

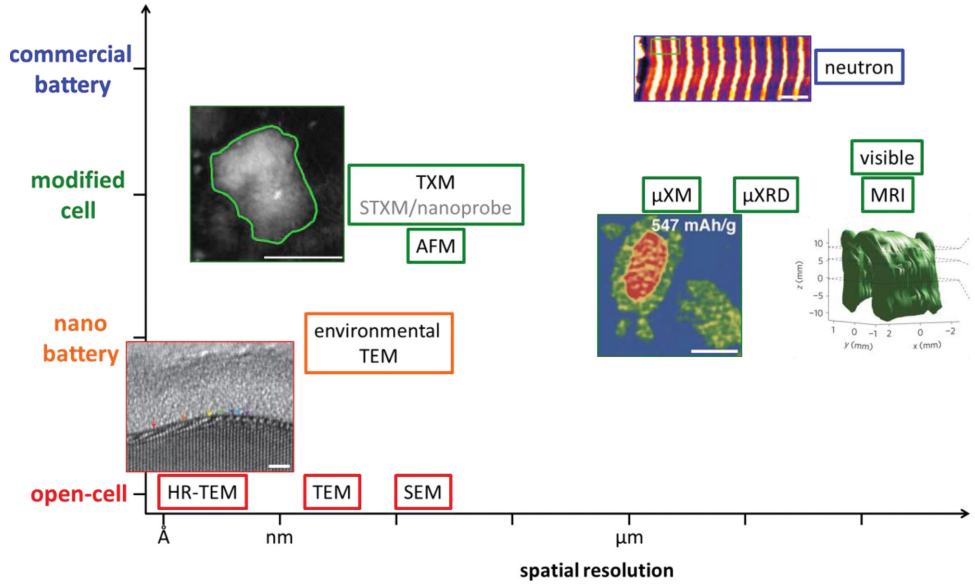

Figure 2. Plot of different in situ imaging techniques for energy storage materials and the type of in situ cell utilized, ranging from commercial batteries to open-cells with ionic liquid or solid electrolyte. As imaging resolution is improved to study finer structures, the required modifications to the in situ cell take it further from a realistic commercial battery architecture. Scalebars are 2 nm, 10 μm, 20 μm, and 500 μm for the HR-TEM, TXM, μXM, and neutron imaging, respectively. Images are adapted from the following. Adapted with permission.[42] Copyright 2012, Macmillan Publishers Ltd: Nature Nanotechnology. Adapted with permission.[24] Copyright 2012, American Chemical Society. Reprinted with permission.[30] Copyright 2013, AAAS. Reproduced with permission.[62] Copyright 2011, The Electrochemical Society. Adapted with permission.[17] Copyright 2012, Macmillan Publishers Ltd: Nature Materials.

Magnetic resonance imaging (MRI)[17] is a valuable approach to probe lithium, but with tens or hundreds of micrometers resolution. Most importantly, over past few years, in situ TEM has been developed for specific cell implementations, discussed in Section 3 below. The use of X-ray based microscopies (full field transmission X-ray microscopy (TXM) and scanning transmission X-ray microscopy (STXM)) for energy storage has only recently emerged.[18] The goal of this article is to provide a perspective on these novel X-ray imaging techniques, particularly for operando and in situ battery studies within the context of the more established probes mentioned above.

Following this introduction, we explain X-ray microscopy (XM) techniques and the morphological, chemical, and structural imaging modalities, including sample cell design considerations. Then, operando and in situ examples of morphological and chemical/structural imaging of energy storage electrodes in both two and three dimensions are presented. We then put XM in perspective with a short description of TEM, and discuss the complementarity of these techniques. This is followed by mention of some emerging X-ray based techniques and a perspective on the future role of XM in energy storage research.

2. X-Ray Microscopy

X-ray microscopes can provide nondestructive, high resolution (tens of nanometers) X-ray images.[19] Although equivalent resolution can be achieved using either a lab- or synchrotron-based

Table 1. In situ characterization techniques used to study energy storage materials and the information that can be tracked by each method. The techniques are grouped by their probe: X-rays, electrons, neutrons, and magnetic.

	Chemistry	Elemental content	Crystal structure	Morphology	Interfaces (SEI)
X-ray diffraction			✓		
X-ray absorption spectroscopy	✓	✓	✓		
X-ray photoelectron spectroscopy	✓	✓			✓
X-ray microscopy	✓	✓		✓	
Electron microscopy		✓	✓	✓	✓
Neutron diffraction			✓		
Neutron imaging				✓	
Nuclear magnetic resonance	✓				
Magnetic resonance imaging				✓	

X-ray source, image acquisition times are at least an order of magnitude shorter with the latter and elemental/chemical imaging is possible with the high flux and energy tunability of a synchrotron source. The two most common X-ray microscopy techniques are TXM and STXM; **Figure 3** shows schematically the optical layout for both methods. TXM is a full field technique, which allows the rapid acquisition of images ideal for tomographic imaging and chemical mapping by means of X-ray absorption spectroscopy (XAS). A relatively large and incoherent X-ray beam is focused onto the sample with a condenser lens (Figure 3 top). The beam footprint on the sample defines the imaging field of view. Depending on the X-ray energy and focusing optic, this can range from tens of micrometers to a few micrometers in diameter. The X-rays scattered and transmitted through the sample are collected by the objective lens, commonly a Fresnel zone plate. The objective lens forms a real-space intensity image on an area detector, often a CCD camera. The numerical aperture of the objective lens (e.g., zone plate) typically determines the spatial resolution for TXM.

In contrast, STXM (typically called a nanoprobe for hard X-rays) is a scanning technique, and thus images are acquired pixel-by-pixel. A STXM generally has a much smaller X-ray source (Figure 3 bottom). The beam is focused to a very small spot size by the condenser lens. This spot size ranges from hundreds of to tens of nanometers and commonly determines the resolution of the instrument. The sample is scanned horizontally and vertically through the X-ray beam, and the intensity of the transmitted light at each sample position is recorded on a point detector. In this manner, an image is built up pixel-by-pixel. Although the acquisition time per image is considerably slower, STXM has the advantage of a flexible field of view and lower radiation dose to the sample (because zone plate lens are about 10% efficient and unlike STXM, TXM has a lens after the sample). STXM allows for elemental or chemical mapping through the detection of fluorescence X-rays or Auger electrons. Similar to TXM, chemical mapping can be achieved by means of XAS. STXM also has the potential for ultra-high resolution (≈1 nm) imaging with ptychography,[20] although this imaging technique is still under considerable development with respect to its application for in situ and operando imaging of energy storage materials (see Section 4).[21]

An arguably more important division of X-ray microscopy than the scanning vs full field delineation is the choice of X-ray energy range. The X-ray energy determines resolution limits, depth of foci, sample thicknesses, available environments, and working distances. Microscopes which utilize hard X-rays (typically defined as > about 6 keV) tend to have slightly lower resolution (25–50 nm) due to the difficulty in fabricating efficient, high resolution hard X-ray optics. However, with hard X-rays the depth of focus is tens of micrometers and these X-rays can penetrate micrometers or even millimeters into solid materials, and these microscopes can operate in air. The focal lengths of hard X-ray lenses are centimeters in length which allows for much larger working distances. This is especially important for operando imaging and tomography of planar samples. Soft X-rays (< about 2 keV) typically have slightly higher resolution (12–40 nm); however the depth of focus is below 10 micrometers. Moreover, soft X-rays are less penetrative so sample thickness can be problematic, and these microscopes typically operate in vacuum or helium. Finally, the focal lengths of soft X-ray lenses are millimeters in length, severely limiting the working distance of the sample. Presently, due to the complexity of soft X-ray microscopy, all in situ and operando, high resolution X-ray microscopic studies on batteries have been performed with X-ray energies at or above 6 keV.[18,22–29]

To map the evolution of the local electrochemical state of an electrode with X-rays, an X-ray absorption edge for a specific element undergoing oxidation or reduction within the active material must be probed (see Section 2.2 for a detailed discussion of chemical imaging). Therefore, when deciding the X-ray energy range to use, the absorption edges that fall within that range should be considered. For example, accessing battery chemistry at the oxygen (543 eV) and carbon (284 eV) X-ray absorption K edges would be extremely informative, especially in studies of the solid-electrolyte interface (SEI) and Li-air batteries. However, due to very soft X-ray energy, the lithium absorption edge (55 eV) is realistically impossible to probe operando with X-ray microscopy. Nevertheless, all of the first row transition metals important in battery technology such as Ni, Mn, Co, Fe, and Zn have K-shell absorption edges in the hard X-ray regime and L edges in the soft X-ray regime and are thus well studied.

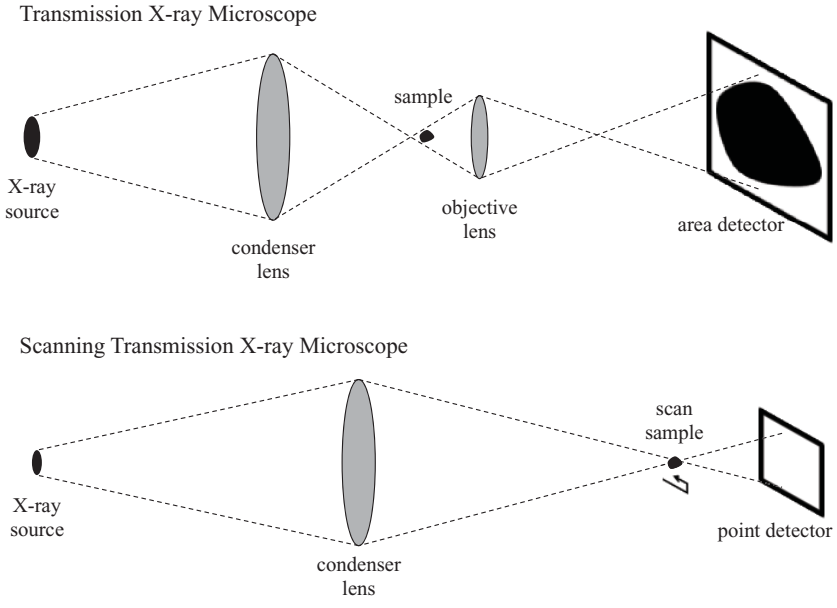

Figure 3. Schematics of the transmission X-ray microscope and scanning transmission X-ray microscope. Not to scale, since the source-lens distance is 10s of meters, while the lens-sample and sample-detector distances are typically a few to 100s mms. For TXM, the objective lens images the sample onto the CCD at a finite distance from the sample and so the sample is not at the focus.

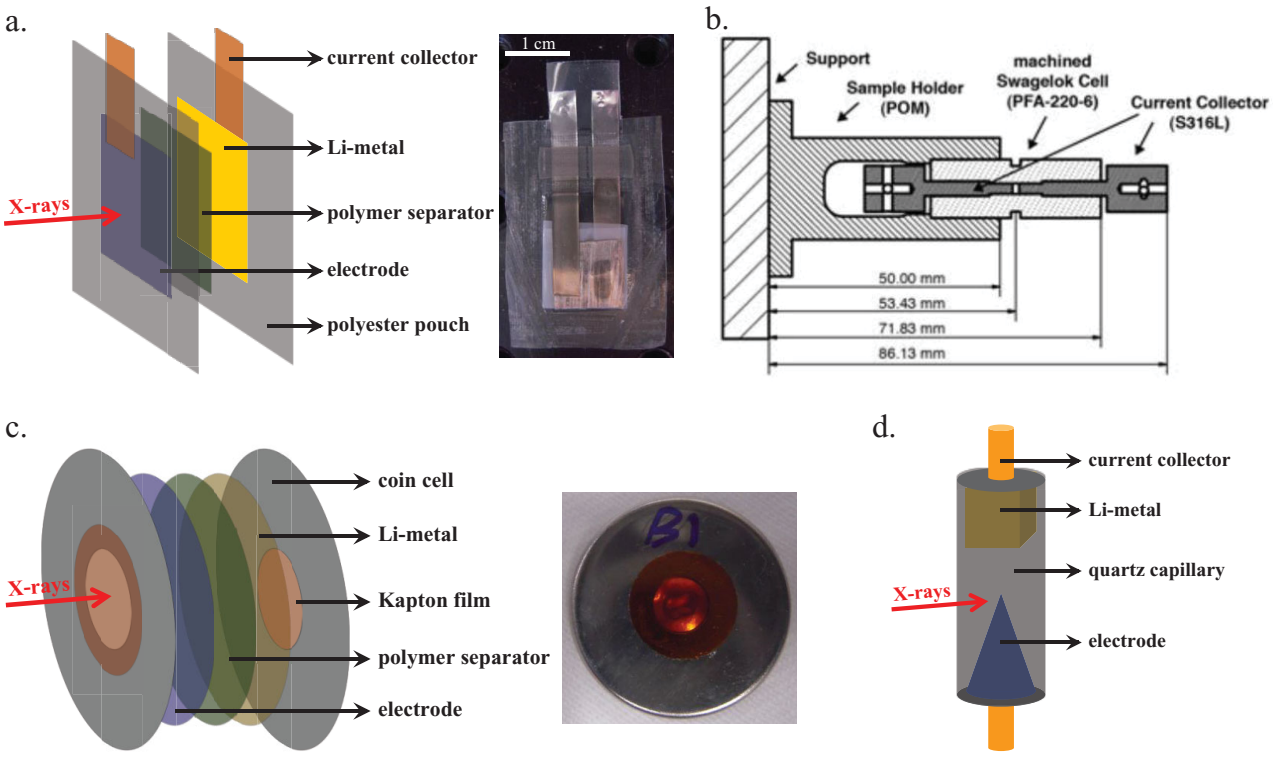

Figure 4. Schematics and images of different operando X-ray microscopy battery cells: a) modified pouch cell using a heat seal polyester pouch,[24] b) Swagelok cell modified for tomography, (Image reproduced with permission.[30] Copyright 2013, AAAS.), c) modified coin cell with imaging holes sealed with Kapton film,[18] Si_3N_4, or Be windows,[31] and d) capillary-based cell ideal for tomography.[26] Operational aspects of the cells (e.g., current collectors, electrodes) are indicated.

A number of variations of operando X-ray microscopy electrochemical cells have been designed (**Figure 4**).[22,24,26,30,31] Many of the cells are modifications of standard electrochemical cells used in the laboratory (pouch, Swagelok, and coin cells). Each has been modified to minimally absorb hard X-rays allowing an unobstructed view of the electrode of interest. For three-dimensional (3D) tomographic imaging, the Swagelok (Figure 4b)[30] and capillary-based (Figure 4d)[32] cells are optimal because they provide an unobstructed view of the electrode through an entire 180° rotation. Planar samples such as the pouch cell (Figure 4a)[24] can be used for tomographic imaging; however, a missing angular wedge can create additional artifacts and would require the use of more sophisticated reconstruction algorithms.[33]

2.1. Morphology

2.1.1. Alloying Electrodes

Alloying electrode materials such as Si, Ge, and Sn and their metal-oxide counterparts such as SnO and SnO_2 are an attractive subset of anode materials to study with operando microscopy because of their extremely large capacity (for Si up to ten times higher than carbon-based anodes) and their dramatic morphology and volume changes to accommodate the large Li-ion insertion. It is therefore no surprise that these materials were some of the first to be studied with in situ AFM,[15] in situ TEM using an ionic liquid[34] or solid electrolyte[35] or standard nonaqueous electrolyte,[36] and operando TXM.[18]

The dramatic volume changes undergone by alloying anode materials are their greatest boon and potential downfall, since the greater the volume expands the more Li ions are inserted. Thus, Si, Ge, and Sn anodes have exceptional theoretical gravimetric and volumetric capacities when compared to currently used graphite electrodes.[37] However, they suffer from fracturing and pulverization resulting in the loss of electronic contact leading to capacity fading and eventual battery failure.[38] Although there are some differences between these materials,[39] studying the failure mechanisms of individual materials can lead to a more complete understanding of this entire class of high capacity anode materials,[37,40] aiding in narrowing the list of desirable potential anode materials.

Recently, Si nanowires and nanoparticles, and to a lesser degree similar Sn, SnO_2, and Ge nanostructures, have been studied using an in situ open-cell TEM geometry.[34,35,39,41–44] However, this cell geometry has aspects that are artificial. Recent studies have demonstrated a more realistic in situ battery cell geometry using a liquid cell.[36,45] A brief comparison of in situ TEM and X-ray microscopies appears in Sec 3. Both the open and liquid cells for in situ TEM allow for the imaging of individual nanostructures. Yet, to image assembly of particles in a tens-of-micrometer thick electrode, operando X-ray microscopy is favored. Chao et al. initially demonstrated the advantages of operando 2D TXM, and used the technique to compare

and contrast the electrochemical lithiation mechanisms of Sn, SnO, and SnSb anode materials.[18,22,23] With operando TXM the evolution of core/shell morphologies was observed in Sn and SnSb particles, and the formation of Sn nanoparticles was identified in both SnSb and SnO micrometer sized particles. From these studies, the authors concluded formation of porous structures allowed fast lithiation/delithiation kinetics and mitigated some of the volume changes inherent to these materials.

2.1.2. SnO Conversion and Alloying Electrodes

2D imaging is sufficient for identifying density changes in electrode materials and observing fracturing and pulverization of particles due to large volume changes. However, to quantify volume changes and verify the complete fracturing of a particle into multiple pieces, 3D imaging is necessary. Ebner et al. have performed operando X-ray tomography with 2-μm resolution on uniform ≈10 micrometer SnO particles with 28 keV X-rays using a Swagelok cell (Figure 4b).[30] Due to the large field of view and speed of data collection (15 minutes per tomography set), all particles in the entire 1.6 mm diameter electrode were imaged operando. Data were recorded during galvanostatic reduction (lithiation) at C/12 and during oxidation (delithiation) at C/5 (100 mA-hour/gm and 167 mA-hour/gm, respectively). Volume expansion of active particles was observed to drive the volume expansion of the entire electrode; however, after the electrode approximately doubled in size, its expansion no longer kept pace with the volume expansion of the particles. The expanding particles began to occupy a greater percentage of the total electrode volume, distorting the inactive carbon and binder permanently. By plotting the normalized attenuation coefficient histograms during cycling, chemical information was deduced. The reduction of SnO to Li_2O + Sn, further reduction to Li_2O + $Li_{4.4}Sn$, and oxidation back to Li_2O + Sn were visualized within individual particles as well as for the bulk. This average bulk behavior is seen in the attenuation coefficient histogram distribution vs capacity plot in **Figure 5**, where the phase sequence is along the capacity curve shown. Individual particles displayed a core/shell reduction reaction. Finally, cracks were seen to develop on opposing sides of particles along parallel grain boundaries, leading to the formation of a zigzag morphology.

Importantly, this study identified the major cause of the capacity loss in this material. This loss is due to the permanent distortion of the conductive matrix by the expanding electrode particles leading to electrical disconnect of the particles and also due to the particle fracturing.

2.1.3. Ge and Sn Anodes

In situ nanometer resolution X-ray tomography has been demonstrated at key points during electrochemical cycling on a Sn anode in a capillary-based cell (Figure 4d)[32] and on a Ge anode in a pouch cell.[29] The capillary-based cell, in comparison to the pouch cell, allows data collection through a full 180° angular range. However, the capillary geometry requires Li-ions to travel a significantly longer path length through the electrolyte than

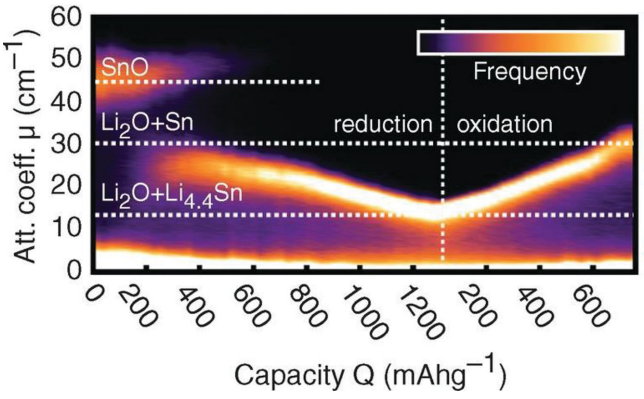

Figure 5. Normalized attenuation coefficient from tomographic reconstructions of an SnO electrode during galvanostatic reduction (at C/12) and oxidation (at C/5). After oxidation the electrode does not return to SnO. Intensity indicates the frequency of pixels with a particular attenuation coefficient. Dashed lines indicate the expected attenuation coefficients for Sn, Sn+Li_2O and Li_2O+$Li_{4.4}Sn$. Reprinted with permission.[30] Copyright 2013, AAAS.

the standard battery cell geometry with just a thin (a few tens of micrometers) separator between the electrodes. The planer geometry of the pouch cell (Figure 4a)[24] allows for approximately a 140° angular range for imaging.

The volume renderings of the tomographic reconstruction of Ge particles and corresponding cross sections are given in **Figure 6** showing the particle morphology and density (a and d) before cycling, (b and e) after the first lithiation, and (c and f) after the first delithiation.[24] Cells were cycled at a constant rate of C/5 and a potential window of 0.0 to 2.0 V vs Li/Li$^+$. The resolution is approximately 50 nm. Cracks can be seen during lithiation (arrows) that lead to a fracturing of the largest particle. **Figure 7** plots the Ge density changes within a subvolume of the upper right Ge particle and shows that after lithiation the Ge density is consistent with the particle partially in the $Li_{15}Ge_4$ state. Delithiation results in almost complete recovery of the pure Ge density, but with a significant tail towards lower density due to incomplete delithiation of some fraction of the particles. The average volume expansion across the three regions studied is ≈315% of the original volume. This is significantly closer to the theoretical value (370%) than observed with in situ TEM of nanoparticles (≈260%).[39] Under the same conditions, one would expect nanoparticles to lithiate more completely than micrometer-sized particles. The smaller volume expansion observed for TEM could arise from the 2D nature of the TEM study, where expansion in the third dimension is unknown.

Using the same pouch cell geometry and Ge electrode composition, 2D operando TXM was performed for the first two electrochemical cycles between 0.0 and 2 V (vs Li/Li$^+$) at C/5. Most notably it was found that during the second cycle the small and medium sized particles did not show any volume change, suggesting that they had become electronically disconnected due to deformation of the electrode's carbon/binder matrix.[29] These results are consistent with the irreversible deformation of the inactive carbon and binder observed by Ebner et al. in SnO electrodes.[30]

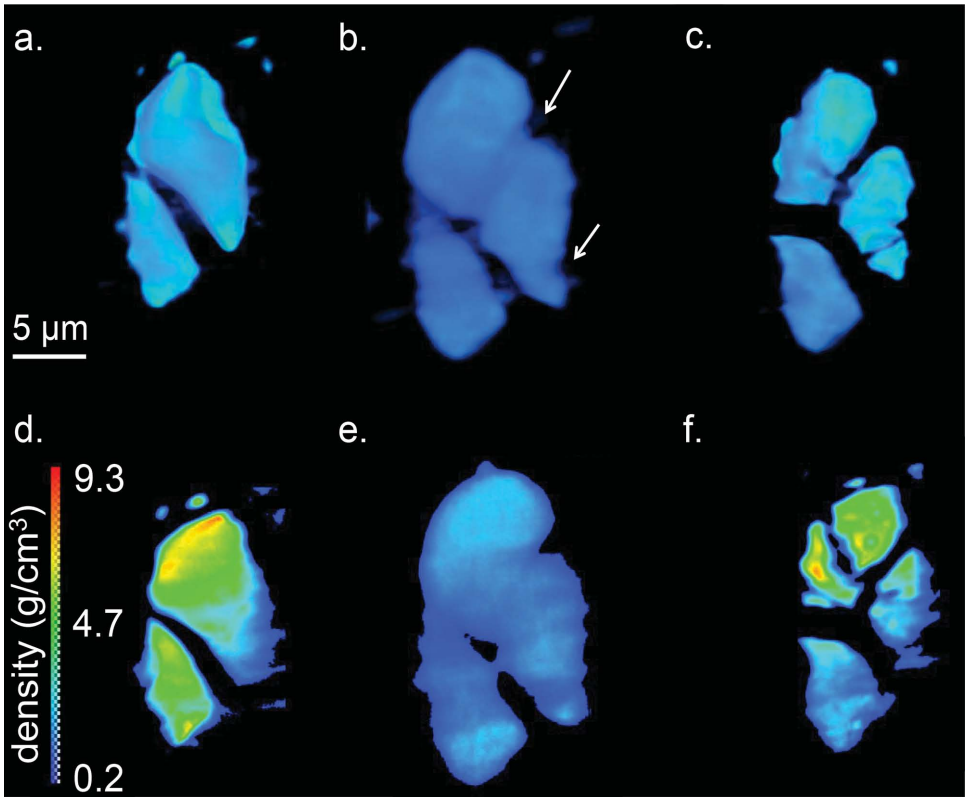

Figure 6. Volume renderings and corresponding cross sections of tomographic reconstruction of a Ge particle a,d) before cycling, b,e) after the first lithiation, and c,f) after the first delithiation. The arrows show cracks that form during lithiation (b); these initiate fracture of the large particle. Cells were cycled at a constant rate of C/5 based on the theoretical capacity of Ge (1600 mA-h/gm) and a potential window of 2.0 V to 0.0 V (Li/Li+). Because of the higher than typical carbon loading, the total cell capacities slightly exceeded the theoretical as lithium was inserted into the carbon. Images reprinted with permission.[29] Copyright 2014, The Royal Society of Chemistry.

Thus, these results on Ge and SnO electrodes show that much of the capacity fade in these alloying electrodes is due to the deformation of the electrode binder, which causes electrical disconnection of the alloying particles. This suggests that some of the capacity fade can be eliminated with approaches to keep the binder in contact with the particles.[46]

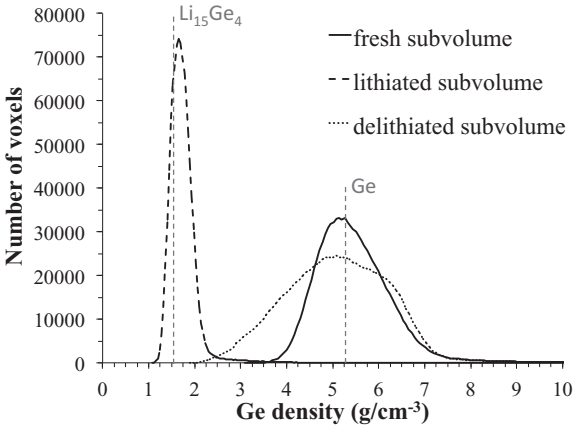

Figure 7. Plot of Ge density histogram within a 2.2 μm × 2.2 μm × 2.2 μm subvolume taken from entirely within the upper right particle in Figure 6 a-c. The Ge densities for pure Ge and $Li_{15}Ge_4$ are displayed as vertical dashed lines. Adapted with permission.[29] Copyright 2014, The Royal Society of Chemistry.

2.1.4. LiS Cells

Although 3D operando imaging reveals more information, it is often sufficient to capture morphological changes in 2D, which benefits from significantly lower dose and simplified geometric constraints. A recent operando TXM and XRD study on a composite sulfur battery demonstrated the overwhelming benefit of characterizing batteries during cycling.[24] Operando XRD can capture metastable phases which only form under active biasing, or confirm the lack of stable phases which would form only after relaxation. Operando TXM allows the imaging of material within macroscopic cells that are actively cycling in a typical geometry and bathed in the standard nonaqueous electrolyte. This is especially critical when studying the interaction of active material and the electrolyte.

Lithium-sulfur batteries have high specific energy and are inexpensive, nontoxic, and earth-abundant. However, significant capacity fading over tens of cycles limits the current functionality of Li-S batteries for commercial use. The primary failure mechanism is believed to be rooted in the solubility of long chain lithium polysulfides, Li_2S_x ($8 \leq x \leq 4$), which form during the discharge cycle, in the electrolyte. Dissolved Li_2S_x

leave the cathode and can even diffuse through the separator and react directly with the Li metal anode. This results in irreversible side reactions, which corrode the Li metal and render the polysulfides inactive. Moreover, as the battery continues to discharge, dissolved Li_2S_x, which remain near the cathode, resolidifies as Li_2S, but not necessarily in the original morphology or location. This can lead to the loss of electronic contact between the active material and the cathode current collector.

Operando TXM was used to study Li-S batteries to follow the dissolution and solidification of the active sulfide material during galvanostatic reduction/oxidation at C/8 (approximately 210 mA-hour/gm). Because this failure mechanism is believed to be primarily due to the interaction between the nonaqueous electrolyte and the polysulfide, in situ TEM using ionic liquid or solid electrolyte would not be as informative. Moreover, sulfur tends to sublime with exposure to high vacuum. With operando TXM, it was found that for composite sulfur electrodes, where the sulfur is melted into the carbon matrix during the electrode fabrication process, very little sulfide dissolution was observed during the discharge cycles.[24] In fact, although lithium polysulfides were forming, the majority of the sulfide material remained localized, seemingly trapped by the carbon matrix. This is illustrated in **Figure 8**a–f which shows micrographs of a sulfur composite particle at various potentials along discharge, as marked in the voltage-capacity plot in Figure 8 (bottom right). The fact that the particles do not change size significantly shows that although some polysulfides diffuse into the electrolyte, the majority of the active material is not lost. By calculating the average contrast between the regions of active material and the background, it was determined that the contrast decreased during the first part of the discharge cycle (from 2.4 to 2.2 V vs Li/Li^+, (a–c) in on potential–capacity plot in Figure 8) where the particle decreases in size the most and where the long chain lithium polysulfides are believed to form (see Figure 8, top right). This drop in contrast was attributed to small amounts of lithium polysulfides dissolving in the electrolyte and leaving the cathode. Since the cycle life of these cells is poor, this study shows that even a small amount of polysulfides dissolution leads to capacity fade.

The subtle loss of polysulfides observed with operando TXM dramatically contrasted with findings from ex situ SEM with energy dispersive spectroscopy on the same composite sulfur electrodes. These ex situ images show a complete loss of sulfide material on the electrode after partial discharge. This apparent contradiction is believed to be the result of artifacts from preparation of the electrode for SEM imaging, which involves disassembling the battery and washing the cathode to remove electrolyte.[24]

With additional TXM experiments on sulfur cathodes prepared without melting sulfur into the carbon matrix, it was found that this partial trapping of lithium polysulfides was highly dependent on the cathode preparation.[27] Micrometer-sized sulfur were prepared by ball-milling with conductive carbon and PVDF binder formed lithium polysulfides, and dissolved completely into the electrolyte by the shoulder of the first discharge voltage plateau (≈2.28 V vs Li/Li^+) in the electrochemical plot. This is seen in **Figure 9**a–c, which shows images of particles along the discharge curve (Figure 9d). The complete dissolution of the ball-milled particles (Figure 9c) is near the end of the large, first discharge plateau, as expected, where the conversion from sulfur to soluble, long chain lithium polysulfides (such as Li_2S_4) is complete. Unlike the sulfur electrode prepared by melting the sulfur into the carbon (Figure 8), the sulfur in this electrode was not well trapped within the

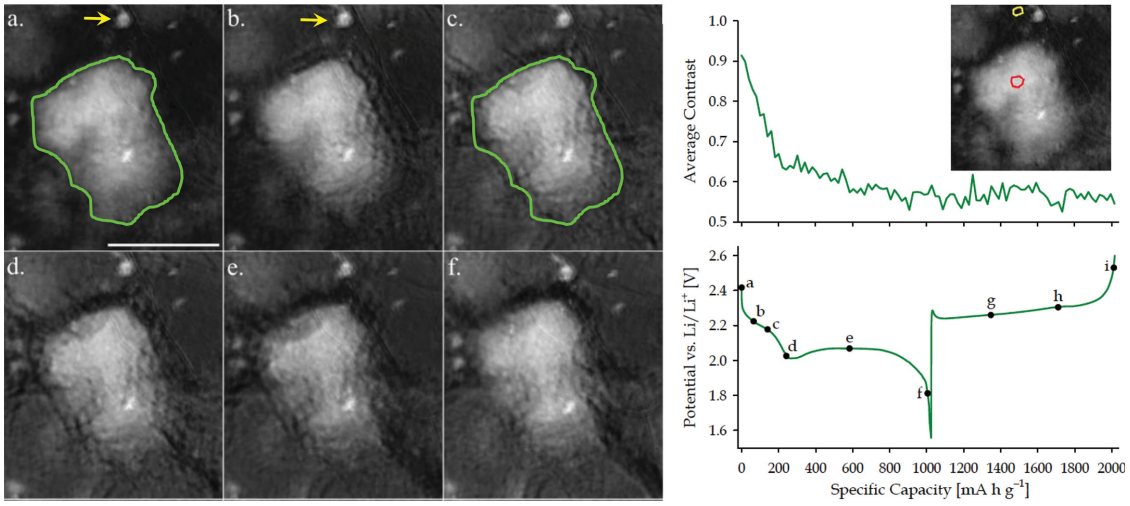

Figure 8. (Left) Operando TXM micrographs of a sulfur composite particle during operation, where the letters correspond to points along the electrochemical cycle labeled a–f on right. The majority of morphological changes occur between images a and c, corresponding to the first plateau of the discharge. The green outline around the particle in (a) is replicated in (c) to show the overall decrease in particle size and increased porosity. The yellow arrows indicate a small particle that expands between (a) and (b). (Right, top) Change in average contrast (difference between light and dark regions) versus specific capacity in TXM micrographs of the Li–S battery cycled at C/8 and (right, bottom) the cell potential. The average contrast was calculated from the image brightness between the average pixel in a small region within a particle and a similarly sized region of the background; averaged for five different particles, each with two different chosen particle and background regions. The inset gives an example of a particle region in red with the background region in yellow. Acquisitions were recorded at 6 keV, scalebar is 10 μm. Image adapted with permission.[24] Copyright 2012, American Chemical Society.

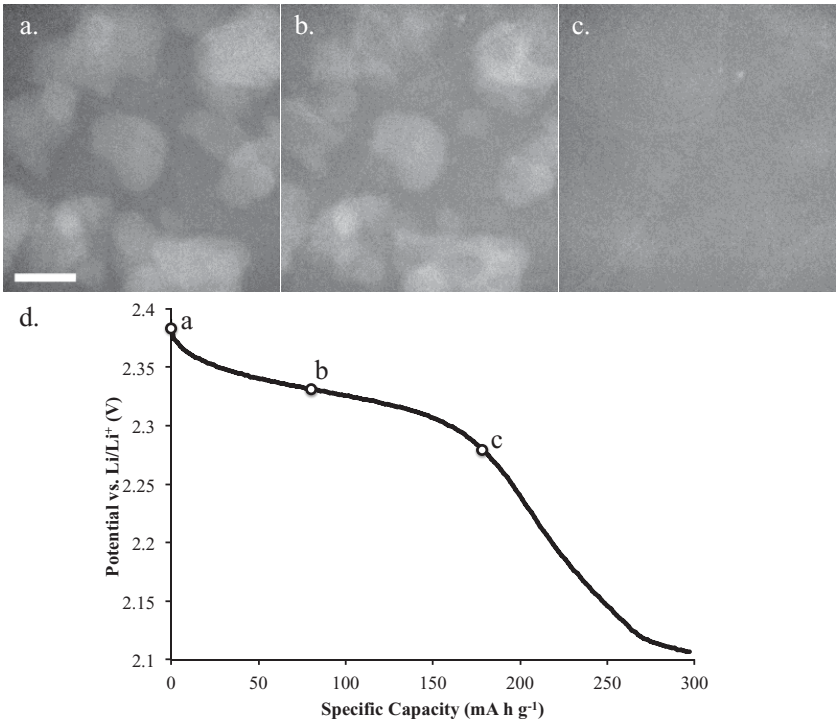

Figure 9. Operando full field TXM images of the dissolution of sulfur particles into the electrolyte during initial discharge (at C/8). By 2.28 V vs Li/Li^+, all sulfur particles (c) have dissolved into the electrolyte as soluble long chain lithium polysulfides. Acquisitions were recorded at 6 keV and the scalebar is 5 µm. Image adapted with permission.[27] Copyright 2013, Society of Photo Optical Instrumentation Engineers.

carbon matrix and was free to diffuse away from the cathode. With operando TXM imaging, the dramatic difference between sulfur cathodes prepared with and without a sulfur-melting step was evident, while ex situ SEM gave no indication that the additional synthesis step improved the rate at which polysulfides left the cathode.

These results are a clear demonstration of the need for operando, high resolution imaging to better understand the failure mechanisms of batteries. They show that the dissolution of the sulfur composition particles is dependent on the cathode particle preparation and that even a small quantity of polysulfides diffusion into the electrolyte can cause capacity fade in Li-S cells. It is necessary to completely trap the soluble polysulfides to improve the cell lifetime. This can be achieved with a more complex sulfur/carbon electrode morphology.[47]

2.2. Chemical and Structural Imaging

Imaging of morphology and volume changes provides only a piece of the electrochemical picture within batteries as they are cycled. Many chemical and structural changes occur without considerable morphological changes. Operando chemical or structural mapping of batteries contributes significant understanding of how different regions or even single particles within an electrode perform, and eventually fail. High resolution chemical imaging can combine X-ray absorption near edge spectroscopy (XANES) with either TXM or STXM. In bulk XANES the absorbed intensity is measured with a fine energy step size (as fine as 0.1–0.2 eV near the edge) and over a large energy range which spans across the absorption edge and well into the extended fine structure after the edge. A typical XAS spectrum is shown in **Figure 10** (for Ni), highlighting the XANES region in light green and in the inset. For chemical imaging, an absorption image is collected at each energy. When properly aligned, the image stack has a XANES spectrum for each pixel in the image. To reduce collection time and radiation dose to the sample, images at only a few to a couple tens of energy points are generally collected (Figure 10 inset). The number of energy points needed is heavily dependent on the differences between the spectra of the expected chemistries within the sample (e.g., points on inset to Figure 10). Chemical imaging has been demonstrated with nanometer resolution in LIB both ex situ,[48–52] in situ (at selected potentials),[25] and operando.[28] Lower resolution chemical or structural maps are possible with microprobes (see for example Nonaka et al. for $LiNi_{0.08}Co_{0.15}Al_{0.05}O_2$)[31] and micro-X-ray diffraction (see for example Shui et al. for Li-air batteries).[53]

2.2.1. $LiFePO_4$ Cathodes

$LiFePO_4$ is a prototypical example of a phase transformation electrode (an insertion electrode—see Figure 1) for Li-ion batteries. In this olivine type cathode, there is a first order electrochemically driven phase transformation from $LiFePO_4$ and $FePO_4$ at about 3.4 V (vs Li/Li^+). As a result, the transformation process in $LiFePO_4$ cathodes has been studied using a wide variety of methods, including recently several XM approaches.

Using both ex situ hard X-ray TXM and soft X-ray STXM, Bösenberg et al. found chemical delithiation to occur more easily at the edges of single crystal $LiFePO_4$ plates, which suggests a process that is not thermodynamically limited, but rather dominated by microstructural features such as voids and cracks.[48] **Figure 11** demonstrates two different means of achieving chemical maps of partly lithiated $LiFePO_4$ plates by probing the Fe absorption edge with hard X-ray TXM (left), where green shows $LiFe^{2+}PO_4$ and red $Fe^{3+}PO_4$, or by probing the oxygen edge with soft X-ray STXM, where the dark regions indicate the presence of $FePO_4$ (right). This ex situ study was limited by the use of chemical delithiation rather than electrochemical delithiation. A complementary ex situ STXM study by Chueh et al. looked at assemblies of electrochemically cycled, nano-sized $LiFePO_4$ particles at about 50% state-of-charge by mapping the Fe L-shell absorption edge.[49] Cells were cycled five times at 1C and then (globally) charged to 50% state-of charge before disassembly. Unlike the micrometer-sized particles, which showed a mixing of the $LiFePO_4$ and $FePO_4$ states

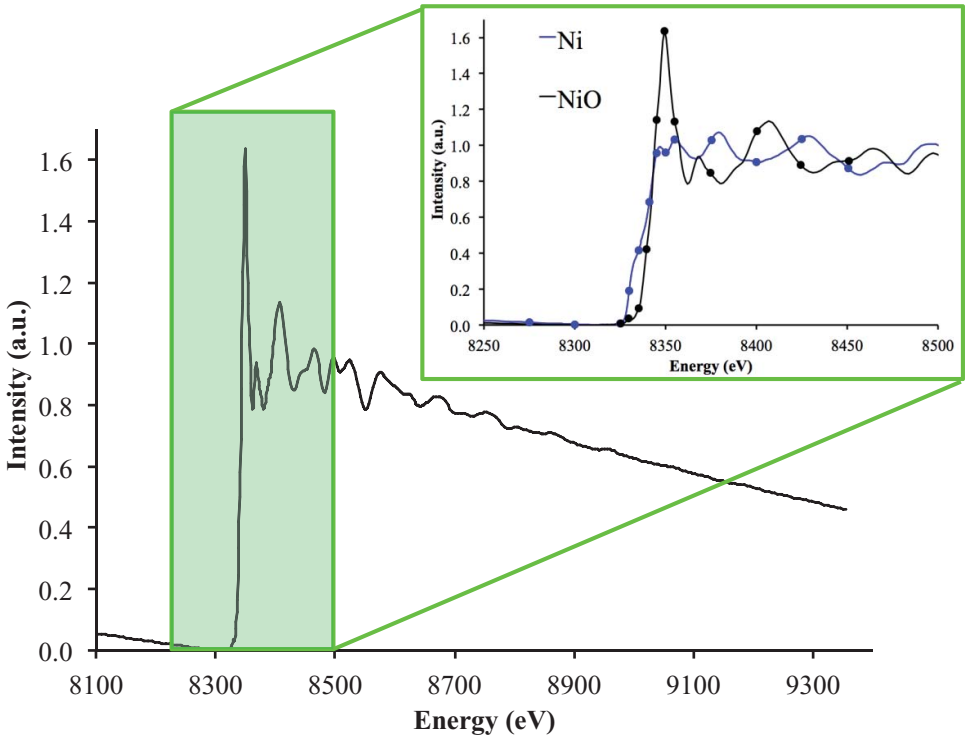

Figure 10. Example NiO X-ray absorption spectrum with XANES region highlighted in green and enlarged as an inset. The inset shows example spectra of Ni and NiO with 13 possible energies (closed circles) at which X-ray imaging could be recorded to confidently distinguish between the two chemical species at the spatial resolution of the microscope. See for example Meirer et al.[51]

with a clear phase boundary, the majority of the nanoparticles were completely in one state or the other as seen by the largely pure red ($LiFe^{2+}PO_4$) or green ($Fe^{3+}PO_4$) particles in **Figure 12**. Only a few particles showed a mix of both phases with a phase boundary traveling linearly rather than radially through the particle (marked with white circles in Figure 12). The yellow regions are overlapping particles.

To fully understand the behavior of the phase boundary within a particle and the particle-particle interaction in assemblies of particles, operando chemical maps are required. Recently, full-field TXM was used to chemically image operando agglomerates of nanometer-sized $LiFePO_4$ particles to determine rate-dependent reaction pathways within the electrode, and within single micrometer-sized $LiFePO_4$ particles to probe the intraparticle phase transition.[28] A comparison was made of slow and fast rates of galvanostatic charging (C/10 vs 5C) from 3 V to 4.2 V (vs Li/Li^+). The data showed that for slow rates there was a significantly larger percentage of pixels in a mix of the $LiFePO_4$ and $FePO_4$ states throughout charge to 4.2 V, suggesting that transformation of the agglomerates is

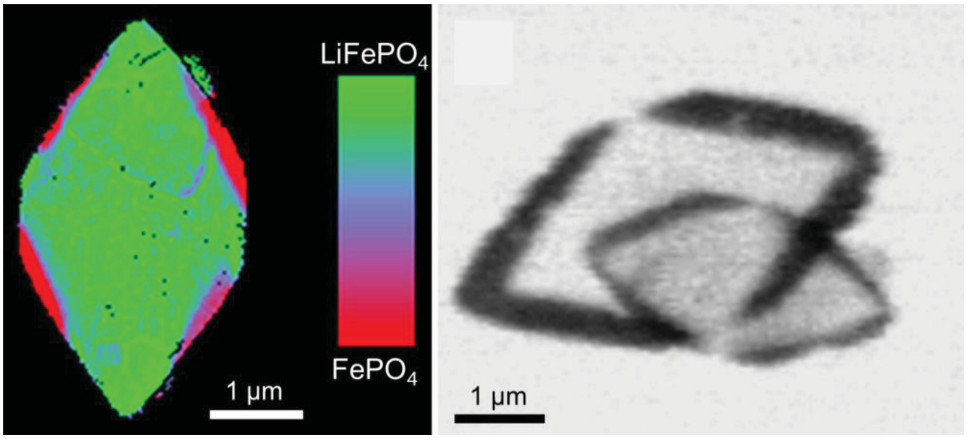

Figure 11. Ex situ chemical map of partly lithiated LiFePO4 plates by probing (left) the Fe K edge with hard X-ray TXM, where the red or dark regions indicate the presence of $FePO_4$, respectively, or (right) the oxygen K edge with soft X-ray STXM, where dark indicates $FePO_4$. Image adapted with permission.[48] Copyright 2013, American Chemical Society.

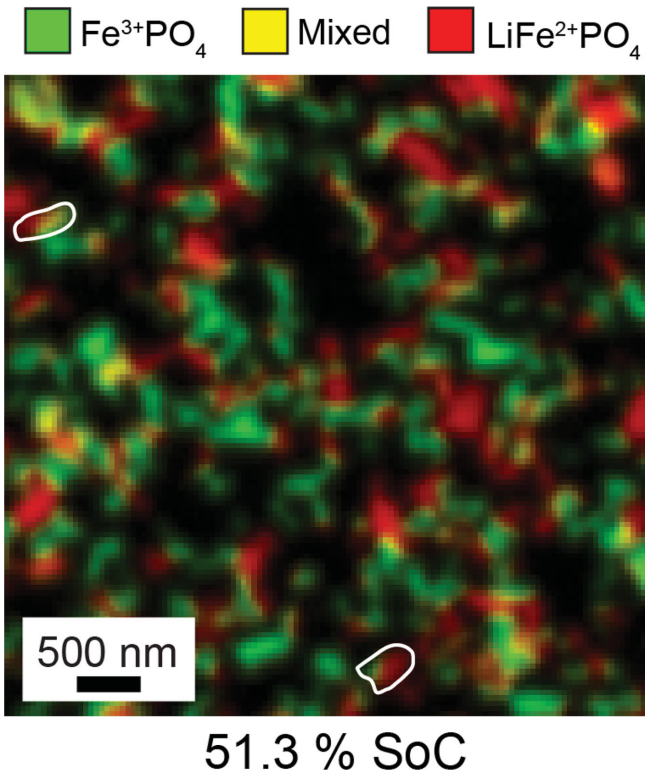

Figure 12. Ex situ chemical maps of assemblies of $LiFePO_4$ nanoparticles at 51% state-of charge. Red shows $Fe^{3+}PO_4$ and green shows $LiFe^{2+}PO_4$. Single particles with two phases (circled in white) were identified using TEM. Clear phase boundaries are visible traversing linearly through these particles. Yellow shows regions where $FePO_4$ and $LiFePO_4$ particles overlap. Image with permission.[49] Copyright 2012, American Chemical Society.

more homogeneous at slow rates, as schematically illustrated in **Figure 13**a. Here red and green indicate pure $LiFePO_4$ and $FePO_4$, respectively, while intermediate colors (orange, light green) are mixed phase. Unfortunately, due to the overlapping of many primary particles, it was not possible to resolve the chemistry of individual primary particles within the micrometer-sized agglomerates, or even to know for certain if the thickness of the electrode contained more than one agglomerate.

By chemically imaging micrometer-size particles, the intraparticle phase transition was tracked during fast (1C) and slow (0.02C) cycling.[28] Two categories of lithium transport through micrometer-sized particles were observed: a one-site transformation pathway and multi-site parallel-direction transport, as indicated in Figure 13b and 13c, respectively. In the first transport model the delithiation pathway extended primarily from one site, while in the second model multiple sites contributed to the transformation. It is unclear whether both or one of these transport models are present in intraparticle phase transitions of nanoparticles, a particle size more typical of commercial $LiFePO_4$ battery electrodes.

Although information on interparticle and intraparticle transport can be gleaned from agglomerates of nanoparticles and individual micrometer-sized particles, operando chemical imaging of a single layer of $LiFePO_4$ particles in the 100-nanometer diameter range would be extremely revealing. However, this is not trivial. Hard X-ray microscopy can probe the Fe K-shell absorption edge, but it would require a STXM with fluorescence detection, such as a hard X-ray nanoprobe, to have sufficient chemical signal on such thin primary particles. The soft X-ray absorption signal at either the O K-edge or the Fe L-edge is strong enough to detect the chemistry of nanometer-sized particles; however, designing an operando transmission cell is challenging. Nevertheless, the design constraints on such a cell would be significantly less demanding than those for TEM, which have already been demonstrated.[36,45] The Auger electron or fluorescence signals could be measured with soft X-ray STXM, but the Auger electron path length would make the technique extremely surface sensitive and the fluorescence signal in the soft X-ray regime is very low.

In summary, XM has shown that there is a rate dependence to the reaction pathway homogeneity in $LiFePO_4$ at a multiparticle level. At slow rates, the phase transformation occurs concurrently, while at fast rates, there are distinct $LiFePO_4$ and $FePO_4$ regions. For nanometer-sized particles, individual particles appear (ex situ) to be mostly single phased (either $LiFePO_4$ or $FePO_4$). Operando XM on a single layer of 100 nm particles is needed to verify this picture, but is challenging.

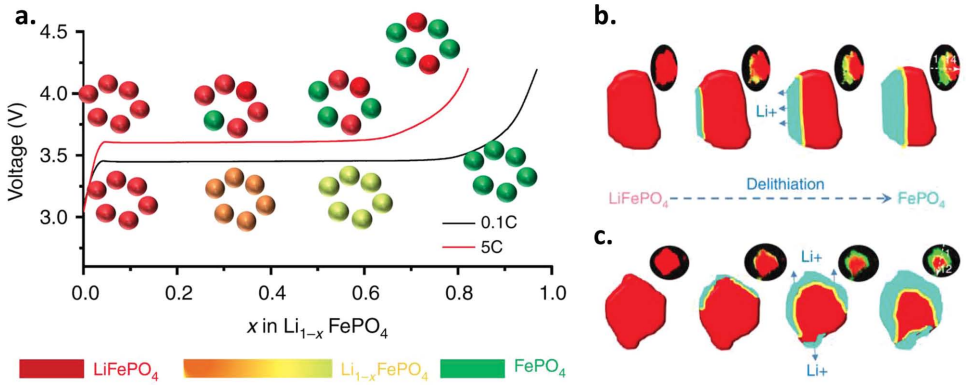

Figure 13. a) Schematic of chemical imaging that shows different phase transformation mechanisms within many nanoparticle agglomerates at fast (top) and slow (bottom) charge rates. Two types of lithium transport through micrometer-sized particles are observed: b) one-site pathway and c) multi-site parallel-direction transport. Images adapted with permission.[28] Copyright 2014, Nature Publishing Group.

2.2.2. NiO Electrodes

Unlike $LiFePO_4$, metal oxide electrodes tend to have a dramatic change in the K-shell absorption edge of the transition metal during reduction and oxidation. Therefore, they are excellent candidates for operando chemical imaging. In what follows, the potential of hard X-ray chemical mapping is demonstrated with ex situ 2D and 3D examples on a NiO electrode cycled at C/5. Ex situ 3D elemental mapping combined with 2D chemical mapping will also be presented on a $Li_{1.2}Mn_{0.525}Ni_{0.175}Co_{0.1}O_2$ cathode.

With ex situ 2D chemical imaging Meirer et al.[51] illustrated a clear irreversibility of the NiO lithium-ion battery in the first cycle. The NiO electrode reduced completely to Ni metal, however, the reoxidation to NiO was just over 50% reversible with regions of mixed phase and pure Ni metal phase. This can be seen in **Figure 14**a, which shows the first charge/discharge cycle (at C/5) along with the NiO (red bars) and Ni (green bars) molar fractions determined for the TXM chemical imaging. Figure 14b shows images at different points along the charge/discharge cycle at P (pristine), R1 (partly reduced), R2 (fully reduced), and O (re-oxidized). The imaging also exhibited a large morphological change with micro-size NiO particles pulverizing into nanoparticles after one reduction and oxidation cycle. This ex situ study sheds some light on the chemical and morphological irreversibility of the electrochemical process in NiO batteries and demonstrates the wealth of information that could be gained by 2D operando chemical imaging on this system.

With 3D chemical imaging, it was demonstrated that the electrochemical front generally propagated from the outside of the agglomerate of NiO nanoparticles inward, creating a core/shell structure that is also believed to occur in individual micrometer sized particles.[51] Moreover, by examining reconstructed slices of the volume, it was shown that the electrochemical front also travels through pores, allowing regions within the core of the agglomerate to reduce before the rest of the material. Porosity clearly plays an important role in the reaction font traveling through agglomerates of nanoparticles, and tomographic imaging is fundamental in quantifying the effects of porosity.[54] Therefore, it is not difficult to imagine the benefit that operando chemical tomography would have on studying NiO and other energy storage materials. Perhaps in situ chemical tomography (hopefully under active bias) will be possible in the next few years as data collection and analysis become more automated. However, radiation dose limits on the electrolyte and/or polymer binder will likely prevent full operando chemical tomography of cells with nonaqueous liquid electrolyte. Nevertheless, it is conceivable that operando chemical 3D imaging of solid electrolyte batteries may be both feasible and informative.

In summary, this ex situ study suggested the importance of a core-shell structure and porosity in the propagation of the reaction front in NiO and showed the potential of 3D chemical imaging of energy storage materials with TXM.

2.2.3. $LiMnNiCoO_x$ Cathodes

Although 3D chemical imaging can provide a wealth of information, it can often be too time consuming and the radiation dose can be too large enough to justify. Careful consideration of which energies to use for collection of tomographic data can reduce data collection to just a handful of tomography datasets, but some knowledge of which chemical states are present is required. With many energy storage materials, 3D elemental imaging can already provide substantial information, especially when combined with 2D chemistry. Yang et al. utilized an ex situ multi-modal TXM approach to understand the morphological and chemical changes occurring in

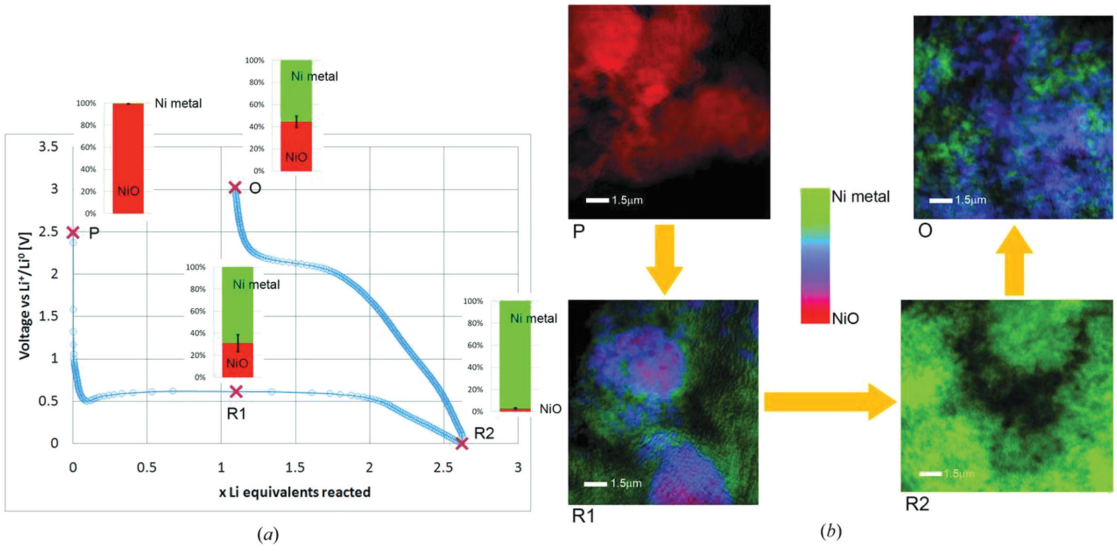

Figure 14. Ex situ chemical X-ray imaging of the reduction and oxidation of NiO electrode from galvanostatic electrochemical cycling at C/5. a) First charge/discharge cycle with bars indicating the chemical composition. b) Chemically resolved images of electrode particles at four points along the charge/discharge cycle: P (pristine), R1 (partly reduced), R2 (fully reduced), and O (re-oxidized). Image reprinted with permission.[51] Copyright 2011, International Union of Crystallography.

$Li_{1.2}Mn_{0.525}Ni_{0.175}Co_{0.1}O_2$ (NMC) cathodes over many cycles.[52] Information from 2D chemical maps of Mn, a statistical analysis of the 3D morphology of many particles, and 3D elemental data on the three transition metals were combined to better understand the chemical and morphological changes occurring with cycling. Coin cells were galvanostatically cycled at C/10 between 2.5 and 4.9 V vs Li/Li^+ for one, 50 and 300 cycles before disassembly. It was found that the Mn chemistry changes with multiple cycling. This is shown in the composition pie charts at the bottom of **Figure 15** obtained from the 3D chemical mapping (images at top of figure). These were obtained from a correlation analysis of the 3D image maps of the 3d metals. The relative compositions show that the pristine particles consist largely of the layered NMC and one galvanostatic charge/discharge cycle (2.5 to 4.9 V vs Li/Li^+) results in 44% MnCoNi (presumably $Li_{1.2-y}(MnCoNi)O_2$), 8% $Mn(Li_yMnO_2)$, and some MiNi and MnCo. After a repeated 200 cycles, the MnCoNi decreases to 37%, while the $Mn(Li_yMnO_2)$ and Ni phases are about 10% with small amounts of other compositions. A similar chemical change was observed after 50 cycles at the particle surface. A statistical analysis of more than 60 particles after one cycle and another set of more than 60 particles after 200 cycles showed an increase in surface roughness (an increased deviation from a spherical morphology) with cycling. Finally, the 3D elemental distribution of particles before cycling, after one cycle, and after 200 cycles, shown at the top of Figure 15, indicate a segregation of the transition metals and a lower transition metal density at the surface after one cycle compared to a pristine particle.

This study showed that when NMC cathode particles are cycling to 4.9 V (vs Li/Li^+) there is a segregation of transition metals changing an initially homogeneous distribution into a more heterogeneous association with depletion near the surface. This change in the surface may partly result in the voltage fade in NMC. This work also demonstrates the wealth of information which can be obtained with XM and with the combination of lower dose studies, such as 2D chemical mapping combined with element-sensitive tomography.

3. Comparison to Electron Microscopy

Here we briefly describe recent approaches using in situ TEM and associated spectroscopic techniques for energy storage electrodes, and contrast these with in situ and operando X-ray microscopies. The goal is not to provide a comprehensive review, but rather to point out the complementarity of these two approaches. Ultimately, a multi-modal approach using both TEM and X-ray microscopies, along with classic electrochemistry, diffraction, spectroscopy, and other existing and emerging techniques, will provide a more comprehensive picture of the storage device operation.

The most prevalent in situ TEM uses an open-cell geometry that requires either an ionic liquid or solid electrolyte rather than the standard non-aqueous liquid electrolyte. The open-cell approach allows for the imaging of individual nanostructures at atomic resolution. Si nanowires and nanoparticles, and to a lesser degree similar Sn, SnO_2, and Ge nanostructures have been investigated using this in situ open-cell geometry.[34,35,42,43] These have shown anisotropic swelling of Si nanowires during lithiation, migration of the 1 nm amorphous-Si_xLi/crystalline-Si interface,[35] and size-dependent fracturing of Si nanoparticles,[41] and have thus provided important insight into atomistic lithiation mechanisms.[42] Most measurements have used a Li_2O solid electrolyte formed onto a Li metal counter-electrode,[34,35,42,43] while several made use of an ionic liquid electrolyte,[34,44] since both these electrolytes have the requisite low vapor pressure. For these open-cells, the cell geometry is considerably different from an actual battery, since the electrolyte does not conformally bathe the electrodes, and the lithiation may occur along a front that travels through the length of the nanowire. The great strength of these open-cell approaches

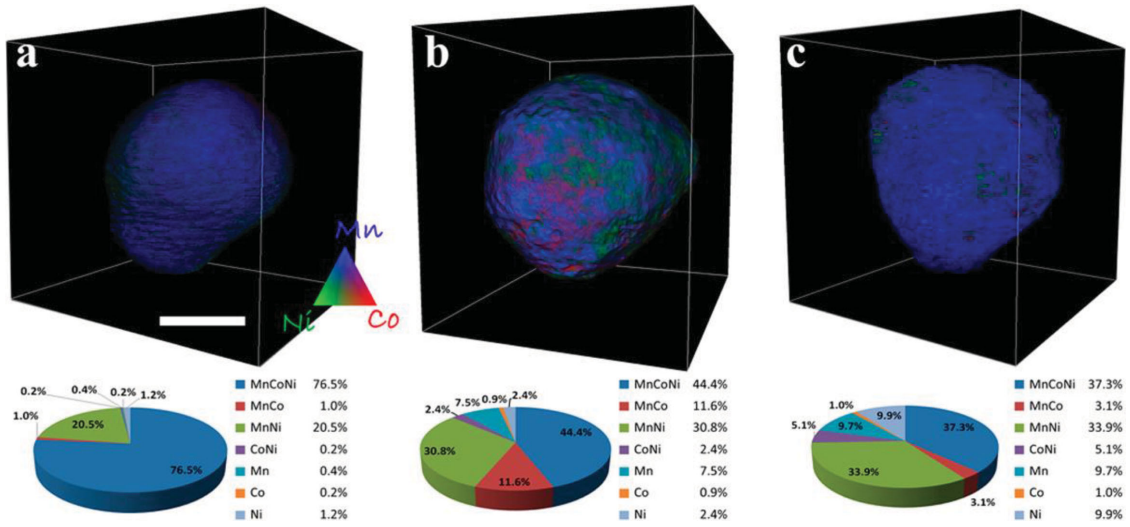

Figure 15. 3D elemental mapping of Mn, Ni, and Co within $Li_{1.5}Mn_{0.525}Ni_{0.175}Co_{0.1}O_2$ particles a) before cycling, b) after one cycle, c) after 200 cycles between 2.5 and 4.9 V vs Li/Li^+ at C/10. The corresponding pie charts indicate the relative concentrations of different groups of elements within the volumes. The pie chart shows the significant changes in Mn chemistry during one cycle and extended cycling. The elemental distribution is indicated with the color legend. The scalebar is 5 μm. Image reprinted with permission.[52] Copyright 2014, American Chemical Society.

is atomic resolution, while the non-realistic geometry is a limitation.

A more realistic in situ TEM battery cell geometry using a liquid cell was recently demonstrated on individual Si nanowires[36] and on $LiFePO_4$ particles.[34] Liquid cells use electron transparent membrane windows to sandwich the electrolyte and electrodes. Liquid cells open up the possibility of studying electrolyte-electrode interactions, especially the solid-electrolyte interface (SEI),[36] which have significant roles in the success or failure of batteries.[55] However, the resolution in the liquid cells was limited to ≈20 nm, most likely due to the low dose necessary to limit beam damage to the electrolyte and the relatively long electron path through the electrolyte.[34,36] While these liquid cells are more realistic, the open-cell approach has the significant advantage that it is much easier to implement and allows for significantly higher resolution imaging.

The heterogeneity across many length scales present in energy storage devices demands a comprehensive, multi-modal approach to characterize and understand their functioning. In this regard TEM, which provide high resolution but in an idealized and restricted experimental geometry, and X-ray microscopies, which entail a more realistic experimental setup but with resolution limited to 20–30 nm, are strongly complementary. In fact, a combination of these techniques, together with other experimental probes, is needed.

4. Emerging Imaging Techniques

There are a few reasonably new, emerging techniques that we briefly note, as these have the potential capability to greatly enhance detailed characterization and hence understanding of energy storage materials. Micro-X-ray diffraction (μXRD) involves structural mapping that combines XRD with a scanning microprobe, with typical resolutions of tens of micrometers. Shui et al. have recently used μXRD to study the structural evolution of Li and LiOH in Li-air batteries with both temporal and spatial resolution in an in situ capillary-based cell.[53]

Coherent diffractive imaging (CDI), in particular Bragg- and transmission ptychography approaches, are emerging, structure sensitive microscopy techniques with X-ray imaging resolution reaching ≈2–5 nm (in the soft X-ray regime), but with a potential of sub-nanometer resolution. In Bragg CDI,[56] coherent scattering patterns are collected from a single particle near a Bragg diffraction peak; the contrast mechanisms include 3D strain. Ptychography combines point scanning with 2D detection of the coherently scattered X-rays.[20] Overlapping spots on a sample are illuminated with a coherent X-ray beam, and extended structures can be imaged with contrast of elemental and chemical composition.[21] Combining both techniques, Bragg ptychography[57] can be used to image strain in 3D on extended structures (e.g., particle aggregates). In these techniques, complicated reconstruction algorithms are used to reconstruct the images.[58] To date, operando Bragg CDI has been reported on $LiNi_{0.5}Mn_{1.5}O_4$ cathode particles during charge/discharge with a resolution of 40–50 nm.[59,60] The 3D strain evolution during the $LiNi_{0.5}Mn_{1.5}O_4$ spinel-spinel phase transformation was imaged in a single ≈300 nm particle. Structural hysteresis was observed in this single particle as were stripes of alternating strain states and coherency strain.[60]

Such experiments are limited by the coherent X-ray fluxes available at present synchrotrons and by detectors with adequate dynamic range and small pixel sizes. However, with the planned implementation in the next approximately five years of sources with factors of 100 to 1000 times higher coherent X-ray fluxes (Advanced Photon Source in the USA, European Synchrotron Radiation Facility, and MAX IV), the resolution will improve significantly (approaching sub-nanometer), although beam damage (likely to electrolyte and/or polymer binder) may become the limiting problem.[61]

5. Perspective on Operando X-Ray Microscopy

In this contribution, we have explained X-ray microscopy and given several examples of operando and in situ morphological and chemical/structural imaging of energy storage electrodes. We contrasted X-ray microscopy (XM) with electron microscopy, illustrating their mutual complementarity, and briefly presented our perspective of future, emerging methods. So far, operando XM has shed light on the degradation mechanisms in Ge and SnO alloying electrodes, provided insight into ways to improve lifetimes in LiS, and informed on reaction pathway homogeneity in $LiFePO_4$. We anticipate that in the near future (≈5 years) the outlook for operando XM is very bright as an increasing number of researchers use this methodology to watch morphological and chemical changes in a diversity of electrode materials, such as nanostructured Si and other newly developed electrodes. This can be seen by the large increase in the number of publications on this subject, since the initial operando XM report in 2012.[24] We expect that new technical XM approaches will appear to address outstanding questions such as electrode state-of-charge. One aspect that needs to be addressed and solved, if possible, is beam damage to the electrolyte and/or polymer binder, which can limit some experiments.[61] It will also be very important to incorporate XM into a true multi-modal (and multi length scale) methodology spanning < 1 nm (atomic) to > 1 μm (cell). This will likely involve a coupling approach with other techniques, such as TEM and tomography, as well as improved, integrated software for modeling these combined data sets.

Further into the future, we anticipate that there will be considerable, continued use of operando XM applied to novel electrode materials as these are developed. Some emerging techniques may overshadow XM, if these methods live up to their potential (e.g., sub-nm resolution), provided that beam damage can be eliminated, or at least mitigated. There may also be some new developments in electron microscopy (EM) that obviate some of the limitations mentioned above that make operando EM widely used for imaging over a large range of length scales.

Acknowledgements

M.F.T. would like to dedicate this Feature to the memory of Joseph Gordon II, who was partly responsible for introducing him to in situ X-ray techniques and electrochemistry. Use of the Stanford Synchrotron Radiation Lightsource, SLAC National Accelerator

Laboratory, is supported by the U.S. Department of Energy, Office of Science, Office of Basic Energy Sciences under Contract No. DE-AC02–76SF00515. This work is partly supported by the Department of Energy, Laboratory Direct Research and Development funding, under contract DE-AC02–76SF00515.

Received: September 29, 2014
Revised: December 16, 2014
Published online: February 4, 2015

[1] a) S. Chu, A. Majumdar, *Nature* **2012**, *488*, 294; b) N. Z. Muradov, T. N. Veriroglu, *Carbon-Neutral Fuels and Energy Carriers*, CRC Press, Boca Raton **2012**.
[2] C.-X. Zu, H. Li, *Energy Environ. Sci.* **2011**, *4*, 2614.
[3] M. S. Whittingham, *Chem. Rev.* **2004**, *104*, 4271.
[4] U.S. D.O.E. EERE, *EV Everywhere: Road to Success* **2014**.
[5] M. R. Palacin, *Chem. Soc. Rev.* **2009**, *38*, 2565.
[6] a) J. Christensen, P. Albertus, R. S. Sanchez-Carrera, T. Lohmann, B. Kozinsky, R. Liedtke, J. Ahmed, A. Kojic, *J. Electrochem. Soc.* **2011**, *159*, R1; b) D. G. Kwabi, N. Ortiz-Vitoriano, S. A. Freunberger, Y. Chen, N. Imanishi, P. G. Bruce, Y. Shao-Horn, *MRS Bull.* **2014**, *39*, 443.
[7] a) K. Amine, R. Kanno, Y. Tzeng, *MRS Bull.* **2014**, *39*, 395; b) K. Kubota, N. Yabuuchi, H. Yoshida, M. Dahbi, S. Komaba, *MRS Bull.* **2014**, *39*, 416.
[8] G. Ceder, G. Hautier, A. Jain, S. P. Ong, *MRS Bull.* **2011**, *36*, 185.
[9] a) M. Balasubramanian, X. Sun, X. Q. Yang, J. McBreen, *J. Power Sources* **2001**, *92*, 1; b) S. Misra, N. Liu, J. Nelson, S. S. Hong, Y. Cui, M. F. Toney, *ACS Nano* **2012**, *6*, 5465.
[10] Y. Arachi, H. Kobayashi, S. Emura, Y. Nakata, M. Tanaka, T. Asai, H. Sakaebe, K. Tatsumi, H. Kageyama, *Solid State Ionics* **2005**, *176*, 895.
[11] L. Cai, Z. Liu, K. An, C. Liang, *J. Mater. Chem. A* **2013**, *1*, 6908.
[12] X.-L. Wang, K. An, L. Cai, Z. Feng, S. E. Nagler, C. Daniel, K. J. Rhodes, A. D. Stoica, H. D. Skorpenske, C. Liang, W. Zhang, J. Kim, Y. Qi, S. J. Harris, *Sci. Rep.* **2012**, *2*, 747.
[13] R. E. Gerald Ii, C. S. Johnson, J. W. Rathke, R. J. Klingler, G. Sandí, L. G. Scanlon, *J. Power Sources* **2000**, *89*, 237.
[14] C. M. Burba, R. Frech, *Electrochim. Acta* **2006**, *52*, 780.
[15] L. Y. Beaulieu, K. W. Eberman, R. L. Turner, L. J. Krause, J. R. Dahn, *Electrochem. Solid-State Lett.* **2001**, *4*, A137.
[16] a) L. G. Butler, E. H. Lehmann, B. Schillinger, *Phys. Procedia* **2013**, *43*, 331; b) D. X. Liu, J. Wang, K. Pan, J. Qiu, M. Canova, L. R. Cao, A. C. Co, *Angew. Chem. Int. Ed.* **2014**, *53*, 9498.
[17] S. Chandrashekar, N. M. Trease, H. J. Chang, L.-S. Du, C. P. Grey, A. Jerschow, *Nat. Mater.* **2012**, *11*, 311.
[18] S.-C. Chao, Y.-C. Yen, Y.-F. Song, Y.-M. Chen, H.-C. Wu, N.-L. Wu, *Electrochem. Commun.* **2010**, *12*, 234.
[19] R. Falcone, C. Jacobsen, J. Kirz, S. Marchesini, D. Shapiro, J. Spence, *Contemp. Phys.* **2011**, *52*, 293.
[20] P. Thibault, M. Dierolf, A. Menzel, O. Bunk, C. David, F. Pfeiffer, *Science* **2008**, *321*, 379.
[21] D. A. Shapiro, Y.-S. Yu, T. Tyliszczak, J. Cabana, R. Celestre, W. Chao, K. Kaznatcheev, A. L. D. Kilcoyne, F. Maia, S. Marchesini, Y. S. Meng, T. Warwick, L. L. Yang, H. A. Padmore, *Nat. Photonics* **2014**, *8*, 765.
[22] S.-C. Chao, Y.-F. Song, C.-C. Wang, H.-S. Sheu, H.-C. Wu, N.-L. Wu, *J. Phys. Chem. C* **2011**, *115*, 22040.
[23] S.-C. Chao, Y.-C. Yen, Y.-F. Song, H.-S. Sheu, H.-C. Wu, N.-L. Wu, *J. Electrochem. Soc.* **2011**, *158*, A1335.
[24] J. Nelson, S. Misra, Y. Yang, A. Jackson, Y. Liu, H. Wang, H. Dai, J. C. Andrews, Y. Cui, M. F. Toney, *J. Am. Chem. Soc.* **2012**, *134*, 6337.
[25] J. Wang, Y.-c. K. Chen-Wiegart, J. Wang, *Chem. Commun.* **2013**, *49*, 6480.
[26] J. Wang, Y.-c. K. Chen-Wiegart, J. Wang, *Angew. Chem. Int. Ed.* **2014**, *53*, 4460.
[27] J. Nelson, Y. Yang, S. Misra, J. C. Andrews, Y. Cui, M. F. Toney, in *X-Ray Nanoimaging: Instruments and Methods*, Vol. *8851* (Ed: B. Lai), SPIE, San Diego **2013**.
[28] J. Wang, Y.-C. K. Chen-Wiegart, J. Wang, *Nat. Commun.* **2014**, *5*, 4570.
[29] J. N. Weker, N. Liu, S. Misra, J. C. Andrews, Y. Cui, M. F. Toney, *Energy Environ. Sci.* **2014**, *7*, 2771.
[30] M. Ebner, F. Marone, M. Stampanoni, V. Wood, *Science* **2013**, *342*, 716.
[31] T. Nonaka, C. Okuda, Y. Seno, H. Nakano, K. Koumoto, Y. Ukyo, *J. Power Sources* **2006**, *162*, 1329.
[32] J. Wang, Y.-c. K. Chen-Wiegart, J. Wang, *Angew. Chem. Int. Ed.* **2014**, *53*, 4460.
[33] D. Verhoeven, *Appl. Opt.* **1993**, *32*, 3736.
[34] J. Y. Huang, L. Zhong, C. M. Wang, J. P. Sullivan, W. Xu, L. Q. Zhang, S. X. Mao, N. S. Hudak, X. H. Liu, A. Subramanian, H. Fan, L. Qi, A. Kushima, J. Li, *Science* **2010**, *330*, 1515.
[35] X. H. Liu, H. Zheng, L. Zhong, S. Huang, K. Karki, L. Q. Zhang, Y. Liu, A. Kushima, W. T. Liang, J. W. Wang, J. H. Cho, E. Epstein, S. A. Dayeh, S. T. Picraux, T. Zhu, J. Li, J. P. Sullivan, J. Cumings, C. Wang, S. X. Mao, Z. Z. Ye, S. Zhang, J. Y. Huang, *Nano Lett.* **2011**, *11*, 3312.
[36] M. Gu, L. R. Parent, B. L. Mehdi, R. R. Unocic, M. T. McDowell, R. L. Sacci, W. Xu, J. G. Connell, P. Xu, P. Abellan, X. Chen, Y. Zhang, D. E. Perea, J. E. Evans, L. J. Lauhon, J.-G. Zhang, J. Liu, N. D. Browning, Y. Cui, I. Arslan, C.-M. Wang, *Nano Lett.* **2013**, *13*, 6106.
[37] D. Larcher, S. Beattie, M. Morcrette, K. Edstrom, J.-C. Jumas, J.-M. Tarascon, *J. Mater. Chem.* **2007**, *17*, 3759.
[38] R. A. Huggins, W. D. Nix, *Ionics* **2000**, *6*, 57.
[39] W. Liang, H. Yang, F. Fan, Y. Liu, X. H. Liu, J. Y. Huang, T. Zhu, S. Zhang, *ACS Nano* **2013**, *7*, 3427.
[40] M. T. McDowell, S. W. Lee, W. D. Nix, Y. Cui, *Adv. Mater.* **2013**, *25*, 4966.
[41] X. H. Liu, L. Zhong, S. Huang, S. X. Mao, T. Zhu, J. Y. Huang, *ACS Nano* **2012**, *6*, 1522.
[42] X. H. Liu, J. W. Wang, S. Huang, F. Fan, X. Huang, Y. Liu, S. Krylyuk, J. Yoo, S. A. Dayeh, A. V. Davydov, S. X. Mao, S. T. Picraux, S. Zhang, J. Li, T. Zhu, J. Y. Huang, *Nat. Nanotechnol.* **2012**, *7*, 749.
[43] a) X. H. Liu, S. Huang, S. T. Picraux, J. Li, T. Zhu, J. Y. Huang, *Nano Lett.* **2011**, *11*, 3991; b) N. Liu, H. Wu, M. T. McDowell, Y. Yao, C. Wang, Y. Cui, *Nano Lett.* **2012**, *12*, 3315; c) A. Nie, L. Y. Gan, Y. Cheng, H. Asayesh-Ardakani, Q. Li, C. Dong, R. Tao, F. Mashayek, H. T. Wang, U. Schwingenschlogl, R. F. Klie, R. S. Yassar, *ACS Nano* **2013**, *7*, 6203.
[44] C. M. Wang, W. Xu, J. Liu, J. G. Zhang, L. V. Saraf, B. W. Arey, D. Choi, Z. G. Yang, J. Xiao, S. Thevuthasan, D. R. Baer, *Nano Lett.* **2011**, *11*, 1874.
[45] M. E. Holtz, Y. Yu, D. Gunceler, J. Gao, R. Sundararaman, K. A. Schwarz, T. A. Arias, H. D. Abruña, D. A. Muller, *Nano Lett.* **2014**, *14*, 1453.
[46] C. Wang, H. Wu, Z. Chen, M. T. McDowell, Y. Cui, Z. Bao, *Nat. Chem.* **2013**, *5*, 1042.
[47] X. Ji, K. T. Lee, L. F. Nazar, *Nat. Mater.* **2009**, *8*, 500.
[48] U. Boesenberg, F. Meirer, Y. Liu, A. K. Shukla, R. Dell'Anna, T. Tyliszczak, G. Chen, J. C. Andrews, T. J. Richardson, R. Kostecki, J. Cabana, *Chem. Mater.* **2013**, *25*, 1664.
[49] W. C. Chueh, F. El Gabaly, J. D. Sugar, N. C. Bartelt, A. H. McDaniel, K. Fenton, K. Zavadil, T. Tyliszczak, W. Lai, K. McCarty, *Nano Lett.* **2012**, *13*, 866.

[50] a) W. M. Harris, G. J. Nelson, A. M. Kiss, J. R. Izzo, Y. Liu, M. Liu, S. Wang, Y. S. Chu, W. K. S. Chiu, *Nanoscale* **2012**, *4*, 1557; b)J. Wang, J. Zhou, Y. Hu, T. Regier, *Energy Environ. Sci.* **2013**, *6*, 926.
[51] F. Meirer, J. Cabana, Y. Liu, A. Mehta, J. C. Andrews, P. Pianetta, *J. Synchrotron Radiat.* **2011**, *18*, 773.
[52] F. Yang, Y. Liu, S. K. Martha, Z. Wu, J. C. Andrews, G. E. Ice, P. Pianetta, J. Nanda, *Nano Lett.* **2014**, *14*, 4334.
[53] J.-L. Shui, J. S. Okasinski, P. Kenesei, H. A. Dobbs, D. Zhao, J. D. Almer, D.-J. Liu, *Nat. Commun.* **2013**, *4*, 2255.
[54] S. J. Cooper, D. S. Eastwood, J. Gelb, G. Damblanc, D. J. L. Brett, R. S. Bradley, P. J. Withers, P. D. Lee, A. J. Marquis, N. P. Brandon, P. R. Shearing, *J. Power Sources* **2014**, *247*, 1033.
[55] P. Verma, P. Maire, P. Novák, *Electrochim. Acta* **2010**, *55*, 6332.
[56] H. N. Chapman, K. A. Nugent, *Nat. Photonics* **2010**, *4*, 833.
[57] a) P. Godard, G. Carbone, M. Allain, F. Mastropietro, G. Chen, L. Capello, A. Diaz, T. H. Metzger, J. Stangl, V. Chamard, *Nat. Commun.* **2011**, *2*, 568; b) I. Robinson, R. Harder, *Nat. Mater.* **2009**, *8*, 291.
[58] S. Marchesini, *Rev. Sci. Instrum.* **2007**, *78*, 011301.
[59] A. Ulvestad, H. M. Cho, R. Harder, J. W. Kim, S. H. Dietze, E. Fohtung, Y. S. Meng, O. G. Shpyrko, *Appl. Phys. Lett.* **2014**, *14*, 5123–5127.
[60] A. Ulvestad, A. Singer, H.-M. Cho, J. N. Clark, R. Harder, J. Maser, Y. S. Meng, O. G. Shpyrko, *Nano Lett.* **2014**, *14*, 5123.
[61] A. P. Hitchcock, M. F. Toney, *J. Synchrotron Radiat.* **2014**, *21*, 1019.
[62] J. B. Siegel, X. Lin, A. G. Stefanopoulou, D. S. Hussey, D. L. Jacobson, D. Gorsich, *J. Electrochem. Soc.* **2011**, *158*, A523.